Biophysical Journal
Article

Biophysical Society

Continuous Dynamic Modeling of Regulated Cell Adhesion: Sorting, Intercalation, and Involution

Jason M. Ko[1] and Daniel Lobo[1,2,3,*]
[1]Department of Biological Sciences and [2]Department of Computer Science and Electrical Engineering, University of Maryland, Baltimore County, Baltimore, Maryland; and [3]Marlene and Stewart Greenebaum Comprehensive Cancer Center, University of Maryland, Baltimore, Maryland

ABSTRACT Cell-cell adhesion is essential for tissue growth and multicellular pattern formation and crucial for the cellular dynamics during embryogenesis and cancer progression. Understanding the dynamical gene regulation of cell adhesion molecules (CAMs) responsible for the emerging spatial tissue behaviors is a current challenge because of the complexity of these nonlinear interactions and feedback loops at different levels of abstraction—from genetic regulation to whole-organism shape formation. To extend our understanding of cell and tissue behaviors due to the regulation of adhesion molecules, here we present a novel, to our knowledge, model for the spatial dynamics of cellular patterning, growth, and shape formation due to the differential expression of CAMs and their regulation. Capturing the dynamic interplay between genetic regulation, CAM expression, and differential cell adhesion, the proposed continuous model can explain the complex and emergent spatial behaviors of cell populations that change their adhesion properties dynamically because of inter- and intracellular genetic regulation. This approach can demonstrate the mechanisms responsible for classical cell-sorting behaviors, cell intercalation in proliferating populations, and the involution of germ layer cells induced by a diffusing morphogen during gastrulation. The model makes predictions on the physical parameters controlling the amplitude and wavelength of a cellular intercalation interface, as well as the crucial role of N-cadherin regulation for the involution and migration of cells beyond the gradient of the morphogen Nodal during zebrafish gastrulation. Integrating the emergent spatial tissue behaviors with the regulation of genes responsible for essential cellular properties such as adhesion will pave the way toward understanding the genetic regulation of large-scale complex patterns and shapes formation in developmental, regenerative, and cancer biology.

SIGNIFICANCE The regulation of cell adhesion molecules (CAMs) is essential for the correct cellular and tissue spatial behaviors during development, and its dysregulation may lead to cancer formation. Here, we show how a novel, to our knowledge, continuous approach can model the spatial dynamics of cell sorting, intercalation, and involution due to differential expression of CAMs. The model explains cell-sorting arrangements and intercalation behaviors, predicting the amplitude and wavelength of the intercalation interface, as well as the involution and migration of germ layer cells during zebrafish gastrulation beyond the gradient that regulates their differentiation. This approach integrates genetic regulation of CAMs, the biophysical forces of adhesion, and the subsequent cellular dynamics to explain how these mechanisms can dictate large-scale tissue behaviors.

INTRODUCTION

The adhesive properties of cells can dictate their spatial behaviors and the formation of correct tissue patterns and shapes during morphogenesis and homeostasis (1). Seminal studies demonstrated how stirred disassociated embryonic tissues could sort themselves and regain their specific configurations because of the distinct adhesive properties of their different cell types (2,3). These cell-cell adhesive forces are dependent on the expression of cell adhesion molecules (CAMs) through the cell surface, such as families of proteins including the cadherins, integrins, and nectins (4,5). CAMs expressed at the cell surface can form bonds with the same or different CAM types expressed in neighboring cells, resulting in different adhesive strengths. These CAM adhesive forces are transmitted to the cell through its cytoskeleton network and can result in specific cell spatial behaviors. The sum of intercellular interactions between different CAMs determines the net force in the cell, which drives specific cellular movements and emergent tissue

Submitted March 19, 2019, and accepted for publication October 22, 2019.
*Correspondence: lobo@umbc.edu
Editor: Stanislav Shvartsman.
https://doi.org/10.1016/j.bpj.2019.10.032

patterns. The importance of cell adhesion is clear when its cellular components are perturbed, resulting in tissues that can degenerate into mispatterned phenotypes during development (6) and disease states such as cancer progression and metastasis (7,8). However, it remains unclear how intercellular interactions between adhesion molecules and the dynamic genetic regulation of their expression can produce these cellular and tissue patterns.

The precise regulation of CAM expression modulates the adhesive properties of cells and hence can control the movement of cells and the formation of global tissue patterns during morphogenesis, whereas its dysregulation may lead to tumor formation and metastasis. Several gene families have been found to regulate CAM expression. The Snail family of transcription factors regulate the expression of cadherins essential for gastrulation in invertebrates, the epithelial-to-mesenchymal transition in neural crest cells in amniotes, and the development of organs such as the kidney (9,10). Differential regulation of CAMs such as cadherins by ephrins and *Hox* genes is a key factor for proper cell distribution during limb morphogenesis and regeneration (11); mutations in these pathways can result in limbs with abnormal morphological organizations (12). Dysregulated pathways controlling CAMs expression are sufficient to induce tumor progression, metastasis formation, and drug resistance (9,13). Kinases can upregulate E-selectin—a CAM essential for the localization of metastatic cancer cells in the lungs (14)—and specific kinase inhibitors targeting these pathways represent promising drugs for anticancer therapeutics (15). However, the complex feedback loops between CAM regulation, cellular adhesion dynamics, tissue behaviors, and intercellular signaling represent an extraordinary challenge that remains to be deciphered.

To understand the complex dynamics between the regulation of CAMs and the spatial tissue behaviors, mathematical and computational approaches are needed to model the physical properties of these processes and explain their emergent dynamics. Discrete models based on the extended Potts approach have been proposed to understand cell adhesion dynamics, and they can recapitulate the classical cell-sorting dynamics due to adhesion (16–18), specific developmental dynamics (19–21), and cancer behaviors (22,23). These models do not include the dynamics of CAM expression and instead use predefined adhesion constants for different cell types. Extensions to these discrete approaches have been proposed to model the concentration of CAMs, using either static concentrations defining cellular adhesion strengths (24) or dynamic concentrations with hybrid models (25). These approaches are based on the explicit modeling of cells and hence computationally expensive for large numbers, which limits their applicability. In addition, discrete models are often not amenable to analytical study with the theory of dynamical systems, including the analysis of their fixed points, bifurcations, and phase portraits. To overcome the limitations of discrete models, continuous models of cell adhesion have been proposed that can equally recapitulate the classical cell-sorting behaviors but are computationally more efficient for the simulation of large populations and amenable for mathematical analysis (26,27). Continuous models have been successfully used to explain developmental processes (28) and cancer dynamics (29–32). However, the adhesion properties in these models are static and defined with specific constants in predefined cell types. As a consequence, the regulation and dynamics of adhesion molecules have not been possible to model with continuous approaches, limiting our ability to understand the regulatory dynamics of CAM expression and their influence in large-scale tissue behaviors such as whole embryos.

Here, we present a novel, to our knowledge, continuous model of cell adhesion due to the expression of CAMs and their regulation. This approach does not rely on predefined adhesion constants between cell types but models as continuous the levels of CAM concentration, which in turn dynamically determine the adhesive properties between cells. Modeling the expression of CAMs naturally allows the inclusion of their regulatory dynamics, which is essential in many biological processes. We demonstrate the capabilities of the proposed model with three experiments. First, we show how the model can correctly recapitulate the classical Steinberg cell-sorting dynamics due to the differential expression of CAMs. Next, we present a model of cellular intercalation dynamics resulting from the differential expression of two different nectins in a proliferating cell population. Finally, we model whole-embryo developmental dynamics during zebrafish gastrulation, explaining how the diffusing morphogen Nodal regulates the expression of a cadherin, dynamically modulating the adhesive properties of cells and resulting in a characteristic involution of the mesendodermal germ layer. Furthermore, the model predicts a robust cell migration toward the animal pole beyond the Nodal gradient. Integrating the regulatory dynamics of CAMs and their cell adhesion properties in the proposed continuous model permits the simulation and spatial predictions of the behaviors of large population of cells due to the interdependent dynamics of genetic regulation and adhesion proteins.

METHODS

Model of dynamic cell adhesion

Model derivation

The dynamic adhesive properties of cells originate from the regulation and expression of CAMs. CAMs expressed on neighbor cells interact with each other, generating adhesive forces. CAMs bind to both CAMs of the same type as well as CAMs of other types. The adhesive force generated from interactions between CAMs hence depends on both the adhesive strength between CAMs and their specific levels of expression in the interacting cells. The dynamic regulation of CAM expression, possibly by intra- and

intercellular regulatory factors, results in dynamic adhesive forces. These dynamic forces can dictate cellular and tissue movement, resulting in target patterns and shapes. The proposed model follows a continuous approach to define a population of cells with adhesion forces as in (26,27), but instead of explicitly modeling cell types, it models types of CAMs (and possibly other factors) expressed in the cells (Fig. 1). The concentration levels of CAMs dynamically give rise to the specific adhesive forces between cells.

We derive the model by considering the forces acting on a population of cells with no proliferation or death to be conservative, which implies by mass conservation

$$\frac{\partial u(\boldsymbol{x},t)}{\partial t} = -\nabla \cdot \boldsymbol{J}, \tag{1}$$

where $u(\boldsymbol{x}, t)$ is the cell density at position $\boldsymbol{x}$ and time t, and $\boldsymbol{J}$ is the flux of the cells. We can rewrite the cell density equation in terms of the flow velocity of the cells, resulting in

$$\frac{\partial u(\boldsymbol{x},t)}{\partial t} = -\nabla \cdot (u\boldsymbol{V}), \tag{2}$$

where $\boldsymbol{V}$ is the velocity field of the cells. Cells contain n different types of CAMs that are advected by the movement of the cells, resulting in

$$\boldsymbol{c} = (c_1, \ldots, c_n),$$

$$\frac{\partial c_i(\boldsymbol{x},t)}{\partial t} = -\nabla \cdot (c_i\boldsymbol{V}), \tag{3}$$

where $\boldsymbol{c}$ is the vector of the n CAM types concentrations $c_i(\boldsymbol{x}, t)$ at position $\boldsymbol{x}$ and time t.

Cells move in a directed manner from regions of high density to those of lower density (27), causing dispersion velocity $\boldsymbol{V_d}$, and toward each other because of adhesive forces between their expressed CAMs, causing adhesion velocity $\boldsymbol{V_a}$, so the total velocity of the cells is

$$\boldsymbol{V} = \boldsymbol{V_d} + \boldsymbol{V_a}. \tag{4}$$

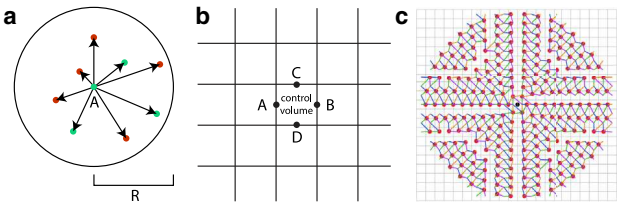

FIGURE 1 Proposed continuous model for the regulatory dynamics of cell-cell adhesion. (*a*) Cells regulate and express different types of adhesion proteins (CAMs, *red* and *green*), causing cell-cell adhesive forces depending on the CAMs concentration in the cells within a radius R. (*b*) A 2D scheme of tissue discretization and cellular fluxes due to dynamic adhesion. Cell density and CAM and other factor concentrations are defined in a grid of discretized control volumes, and the flux is defined across the boundaries between control volumes (points A–D). (*c*) Kernel for the numerical discretization in two dimensions of the adhesion integral at boundary point A in (*a*). The adhesion values are computed at points at regular angular and radial directions (*red circles*) from the boundary point (*black circle* at the *center*), with a bilinear interpolation of CAM concentrations from the center of the four surrounding control volumes (*cyan*, *magenta*, *yellow*, and *green lines*). The same kernel is used for boundary point B, and its transpose is used for boundary points C and D. The example shows a discretization with 42 angular by 10 radial directions. To see this figure in color, go online.

We assume that the cell dispersion velocity is proportional to the population density, which implies

$$\boldsymbol{V_d} = -k_p \nabla u, \tag{5}$$

where k_p is the dispersion constant. Diffusion is assumed to be negligible relative to the strength of dispersion and adhesion (27).

The adhesion velocity vector depends on the adhesive bonds between CAMs expressed in the cells and their neighbors within a sensing radius R (Fig. 1 *a*). This radius models the size of a cell, including their ability to reach and contact other cells through the cell body and through their protrusions such as filopodia. Following Newton's law and assuming that inertia is negligible for cell movements, the adhesion velocity vector is then inversely proportional to the cell radius (because of drag) and proportional to the pairwise sum of all adhesion forces between the n CAM types such that

$$\boldsymbol{V_a} = \sum_i^n \sum_j^n \frac{\phi}{R} \boldsymbol{K}\big(u, c_i, c_j\big)(\boldsymbol{x}), \tag{6}$$

where ϕ is a constant of proportionality related to viscosity, n is the number of CAM types, and $\boldsymbol{K}(u, c_i, c_j)(\boldsymbol{x})$ is the nonlocal cell adhesion force vector at location $\boldsymbol{x}$ due to the bonding interactions between the two CAM types c_i and c_j. The adhesive strength between CAM types are defined by a symmetric square matrix A, where each element a_{ij} represents the adhesion strength between CAM types c_i and c_j, and hence the diagonal defines the homotypic adhesion strengths for each CAM type. The nonlocal cell adhesion force depends on the adhesive bindings between the CAMs expressed in the local cell at point $\boldsymbol{x}$ and those expressed by its neighbors within the cell-sensing radius R. In d spatial dimensions, it takes the form

$$\begin{aligned}\boldsymbol{K}\big(u, c_i, c_j\big)(\boldsymbol{x}) = &\int_0^R \int_{S^{d-1}} a_{ij}\left[f\big(u, c_i, c_j\big)\big(\boldsymbol{x}, \boldsymbol{x} + r^{d-1}\boldsymbol{\eta}\big)\right] \\ &\times\ \omega(r)\, r^{d-1}\boldsymbol{\eta}\, \mathrm{d}\boldsymbol{\eta}\, \mathrm{d}r,\end{aligned} \tag{7}$$

where S^{d-1} is the d-dimensional unit spherical surface; r is the radial distance; $\boldsymbol{\eta}$ is the direction vector; $f(u, c_i, c_j)(\boldsymbol{x}, \boldsymbol{x} + r^{d-1}\boldsymbol{\eta})$ describes the nature of adhesive forces between CAM types c_i and c_j expressed from cell locations $\boldsymbol{x}$ and $\boldsymbol{x} + r^{d-1}\boldsymbol{\eta}$, respectively, and their dependence on the cell density; and $\omega(r)$ describes how the cell adhesive force depends on the radial distance r. For simplicity, we assume $\omega(r) = 1$ in this work.

The adhesive force between two CAM types expressed by two cells depends on their binding activity due to the CAMs' relative concentrations within each cell. We assume that the binding activity follows the law of mass action, such as the adhesive force exerted on cells at location $\boldsymbol{x}$ expressing CAM type c_i by cells at location $\boldsymbol{y}$ expressing CAM type c_j depends on the product of their relative concentrations because the force is calculated per unit of cell density within their respective cells, given by

$$f\big(u, c_i, c_j\big)(\boldsymbol{x}, \boldsymbol{y}) = \frac{c_i(\boldsymbol{x})}{u(\boldsymbol{x})} \frac{c_j(\boldsymbol{y})}{u(\boldsymbol{y})} h(u(\boldsymbol{y})), \tag{8}$$

where $h(u(\boldsymbol{y}))$ represents how the adhesive force depends on the local cell density. As in (26,27), we assume a population pressure that causes cells to be attracted only to regions below a threshold density. For this, a logistic function with crowding capacity k_c limits the cell movement because of adhesion toward dense regions:

$$h(u) = \begin{cases} u\left(1 - \dfrac{u}{k_c}\right) & \text{if } u < k_c, \\ 0 & \text{otherwise.} \end{cases} \tag{9}$$

A nondimensional model is defined by rescaling with

$$x^* = \frac{x}{R}, t^* = \frac{k_p k_c}{R^2} t, u^* = \frac{u}{k_c}, c_i^* = \frac{c_i}{k_c}, A^* = \frac{R\phi}{k_p} A \quad (10)$$

and dropping the stars, we obtain the model

$$\frac{\partial u(\boldsymbol{x}, t)}{\partial t} = -\nabla \cdot (u\boldsymbol{V}),$$

$$\frac{\partial c_i(\boldsymbol{x}, t)}{\partial t} = -\nabla \cdot (c_i\boldsymbol{V}), i \in [1, n],$$

$$\boldsymbol{V} = -\nabla u + \sum_i^n \sum_j^n \boldsymbol{K}\big(u, c_i, c_j\big)(\boldsymbol{x}),$$

$$\boldsymbol{K}\big(u, c_i, c_j\big)(\boldsymbol{x}) = \int_0^1 \int_{S^{d-1}} a_{ij} \left[\frac{c_i(\boldsymbol{x})}{u(\boldsymbol{x})} \frac{c_j(\boldsymbol{x} + r^{d-1}\eta)}{u(\boldsymbol{x} + r^{d-1}\eta)} \times h\big(u\big(\boldsymbol{x} + r^{d-1}\eta\big)\big) \right] \omega(r)\, r^{d-1} \boldsymbol{\eta}\, \mathrm{d}\boldsymbol{\eta}\, \mathrm{d}r,$$

$$h(u) = \begin{cases} u(1-u) & \text{if } u < 1, \\ 0 & \text{otherwise.} \end{cases} \quad (11)$$

Numerical methods

Simulations were computed in a 2D domain using the explicit upwind finite volume method with flux limiting in a uniform square lattice and a zero-flux boundary condition. The nonlocal integral term for adhesion is discretized into angular and radial components using bilinear interpolation. The system was numerically solved using ROWMAP (33) and implemented in MATLAB R2017b (The MathWorks, Natick, MA). Methods are detailed in the Appendix.

RESULTS

We demonstrate the ability of the proposed model to explain tissue shape behaviors due to the differential expression of CAMs with three simulations of in vitro and in vivo experiments. Classical cell-sorting behaviors can be recapitulated in the model in a population of nongrowing cells expressing two different CAM types, resulting in engulfment, mixing, or sorted cellular aggregates depending on the adhesive strengths between the CAM types. Extending the model with cell growth, a simulation of in vitro growing dynamics shows how a proliferating cell population can result in either separated or intercalated patterns because of the cells expressing either the same or different nectins, respectively. Finally, the dynamics of zebrafish gastrulation are explained with an extended model including the expression of a morphogen forming a gradient, which in turn upregulates the expression of the CAM N-cadherin, inducing the involution of these cells because of their acquired differential cell adhesion properties, even beyond the expression gradient of the morphogen. Importantly, the behaviors shown in the simulations are not due to inherent cell adhesion strengths between different cell types but from dynamic adhesion strengths that arise from the concentration of various CAM types, in which each CAM type has specific molecular adhesion values and their concentrations, and hence the resulting cell adhesion forces, can be subject to genetic regulation.

Cell-sorting behaviors

CAM types can bind to each other with different adhesive strengths, so cell-cell adhesion forces depend on the levels of expression of the different CAM types. These differences in cell-cell adhesion can cause an emerging cellular self-organization into different spatial patterns, a behavior shown in vitro in a variety of animal cells, including amphibian (2), chick (34,35), zebrafish (18), and hydra (36). In these experiments, cells express different CAM types with different adhesive properties. Some combinations of CAM types can confer strong adhesive forces, causing cells to bind tightly to each other in the core of the final sorted aggregate. Other combinations of CAM types generate lower adhesive forces, resulting in cells that bind loosely to each other and move to the outside of the aggregate.

The proposed continuous nondimensional model (Eq. 11) can demonstrate cellular sorting behaviors because of the differential expression of CAMs, which are qualitatively similar to in vitro experiments using dissociated zebrafish (18) or transfected CHO cells (37). Fig. 2 shows four different sorting behaviors resulting from nonproliferating cells expressing either of two CAM types with different adhesive strengths (strength values as estimated in (27)). All the simulations start with the same initial random configuration of disassociated tissue, in which each initial aggregate contains cells expressing one of two different CAM types. Depending on the relative strength of the homotypic and heterotypic adhesion strengths between the CAM types, the spatially randomized tissues form aggregates that self-organize into patterns of engulfment, partial engulfment, mixing, or complete sorting. When the CAM homotypic adhesion strengths are asymmetric, the simulation recapitulates the engulfment behaviors observed in vitro (Fig. 2 *a*). This sorting behavior is due to the differential expression of CAMs, in which cellular aggregates expressing the CAM type with stronger homotypic adhesion strength (*red*) are tightly adhered and hence surrounded by the cellular aggregates expressing the CAM type with weaker homotypic adhesion strength (*green*). However, when the homotypic adhesion strengths of the two CAM types are equal but still higher than the heterotypic adhesion strength, no cell aggregate is stronger than the other, and hence, there is still sorting between the tissues expressing the different CAM types

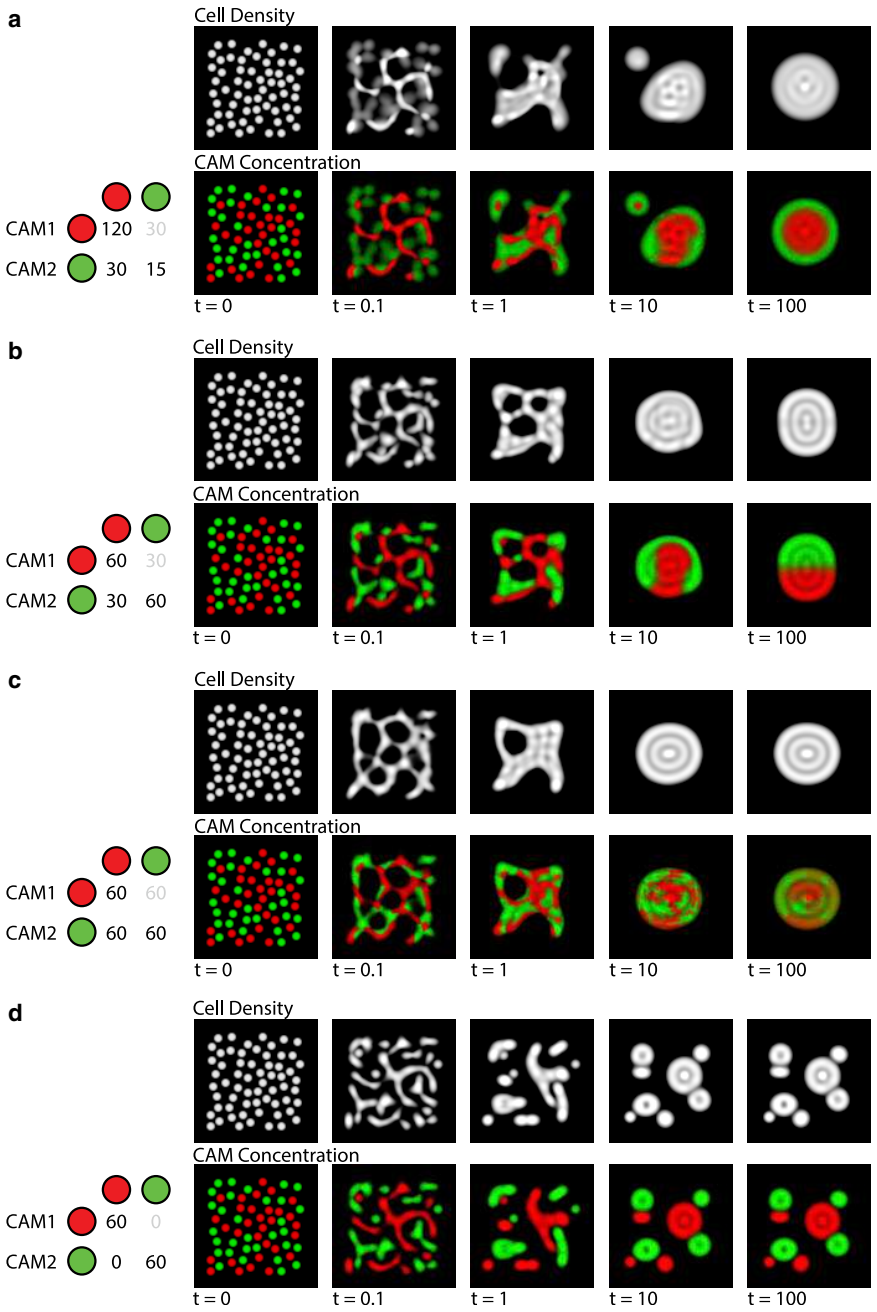

FIGURE 2 Cell-sorting simulations in a population of cells expressing either of two CAM types with different adhesion strengths. (*a*) Asymmetrical homotypic adhesion strengths in the CAM types result in the engulfment of the cells expressing the higher-adhesive-strength CAM type (*red*) by the cells expressing the lower-adhesive-strength CAM type (*green*). (*b*) Symmetric homotypic adhesion strength higher than the heterotypic adhesion strength results in partial engulfment. (*c*) When the homotypic and heterotypic adhesion strengths are equal, the cells become mixed. (*d*) Without heterotypic adhesion forces, the cell populations expressing the two different CAM types completely sort themselves. Matrix diagrams indicate the homotypic and heterotypic adhesion strengths between CAM types. All simulations start with the same initial state of equal red and green CAM type total concentration. Domain is of size 10 × 10 units, discretized into a 100 × 100 grid; arbitrary units. To see this figure in color, go online.

but no engulfment (Fig. 2 *b*). In contrast, the randomized tissues do not sort themselves when the homotypic and heterotypic adhesion strengths are equal (Fig. 2 *c*), resulting in aggregates that are mixed. In the complete absence of heterotypic adhesion between the two CAM types, the tissues sort themselves completely, forming separated aggregates (Fig. 2 *d*). These simulations show how the cell-sorting behaviors depend on the homotypic and heterotypic adhesion strengths between the CAM types and their levels of expression in the different tissues. Cells first aggregate into transient local clusters ($t = 0.1$), which eventually merge into larger aggregates ($t = 1$ to $t = 100$). This dynamic behavior recapitulates both in vitro experiments and previous discrete models (38). Although the specific final steady state depends on the initial state, qualitatively different steady states emerge as the result of the specific adhesion strengths between CAM types (Fig. S1).

Cell intercalation in proliferating cell populations

The spatial tissue behaviors in a population of proliferating cells can depend on both the expression levels and the adhesive properties of CAMs. This has been shown in in vitro

coculture assays of two proliferating cell populations expressing similar or different nectin adhesion proteins (6). When both populations express the same CAM type (nectin-1), the boundary formed between the two populations at the contact plane is well-defined, and the cells do not mix. In contrast, when each population express a different CAM type with different adhesive properties (nectin-1 or nectin-3), the two populations mix and intercalate at the boundary. The proposed model can explain these behaviors because of the differential expression of nectin-1 or nectin-3 in the two proliferating cell populations.

We extend Eq. 2 to include a simple logistic cell growth term $g(u)$ such that

$$\frac{\partial u(\boldsymbol{x},t)}{\partial t} = -\nabla\cdot(u\boldsymbol{V}) + g(u),$$

$$g(u) = k_g u\left(1-\frac{u}{k_k}\right), \tag{12}$$

where k_g is the cell growth rate and k_k is the cell carrying capacity. We assume that the daughter cells continue expressing the same CAM types as their parent cells so that the relative CAM concentration in the daughter and parent cells are equal. In this way, we extend Eq. 3 to

$$\frac{\partial c_i(\boldsymbol{x},t)}{\partial t} = -\nabla\cdot(c_i\boldsymbol{V}) + \frac{c_i}{u}g(u). \tag{13}$$

This extended model can explain the in vitro intercalation dynamics of growing cell populations resulting from the differential expression of CAMs. We use the dimensional parameters as experimentally measured in (27):

$$R = 100\ \mu\text{m},$$

$$k_k = 0.005595\ \text{cells}/\mu\text{m}^2,$$

$$k_g = \frac{1}{12}\ \text{h}^{-1}.$$

The parameter k_c could not be measured experimentally and was set to k_k. We then fitted the model to the experimental images from (27), setting $\phi = 100$ and $k_p = 126{,}000\ \mu\text{m}^2/\text{h}\cdot\mu\text{m}^2/\text{cells}$.

Fig. 3 shows simulations of growing population dynamics when the two cell populations express either the same (nectin-1) or different (nectin-1 or nectin-3) CAM types. The homotypic and heterotypic adhesion strengths of nectin-1 and nectin-3 are derived from protein-protein interaction experimental data measured with surface plasmon resonance (39) and their values are shown in Fig. 3 *a*. Both simulations start with the same initial state for cell density—two random cell populations on the opposite sides of the domain—and homogeneous relative concentration of either nectin-1 or nectin-3 ($a/u = 1$). This random initial state for cell density simulates the noise in biological cells in the deterministic model, which otherwise would result in an unrealistic equilibrium of adhesion forces at the center of the front because of perfectly symmetrical cell densities. During the simulation, the cells proliferate and spread through all the domain up to the carrying capacity density. When both left and right cell populations express the same CAM type (nectin-1), they do not mix or intercalate at the interface because the adhesive forces between the two populations are balanced equally and hence cancel out (Fig. 3 *b*). In contrast, when the two populations express different CAM types (nectin-1 or nectin-3), the difference in homotypic adhesive strengths results in the mixing and intercalation pattern at the interface (Fig. 3 *c*). The simulation hence shows how either intercalation or smooth boundaries can arise at the interface of two growing cell populations depending on the expression levels and adhesive properties of their CAMs.

The model predicts the specific amplitude and wavelength of the intercalation interface depending on the physical parameters. Fig. S2 shows the steady states resulting from individually varying the parameters of the model. Except for the dispersion constant k_p, all other parameters considerably affect the pattern of the intercalation interface. To quantify the effect of each parameter on the intercalation pattern, we measured the amplitude of the interface and caculated its wavelength with a Fourier analysis when perturbing each parameter individually by a factor (Fig. S3). The results show that the intercalation amplitude increases linearly with the sensing radius

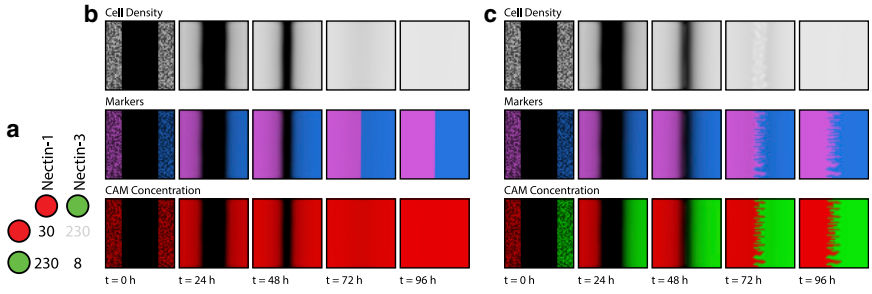

FIGURE 3 Simulation of proliferating cell populations expressing identical or different CAM types explains in vitro intercalation behaviors. The two cell populations express a different marker (*magenta* or *blue*) and either the same or different CAM type (nectin-1 in *red* and nectin-3 in *green*). (*a*) Homotypic and heterotypic adhesion strengths of nectin-1 and nectin-3. (*b*) Cell populations proliferating and expressing the same CAM type, nectin-1, do not mix when they meet at the interface. (*c*) Cell populations proliferating and expressing different CAM types, nectin-1 or nectin-3, mix and form intercalated patterns when they meet at the interface because of the different homotypic adhesion strengths of the two CAM types expressed. Domain is of size 1 × 1 mm, discretized into a 50 × 50 grid. To see this figure in color, go online.

R, the constant related to viscosity ϕ, and cell carrying capacity k_k but decreases exponentially with the dispersion constant k_g. The intercalation wavelength increases linearly with the sensing radius R and, to a lesser extent, with the constant related to viscosity ϕ and cell carrying capacity k_k but decreases linearly with the dispersion constant k_p.

Dynamic regulation of adhesion during gastrulation

During gastrulation, Nodal acts as a diffusive morphogen, forming a concentration gradient that induces mesendoderm differentiation (40). In zebrafish, Nodal is expressed in the yolk syncytial layer (YSL), a region of the yolk consisting of nuclei that have descended from the blastoderm (41). The YSL is divided into two segments: the internal YSL (iYSL), which is completely covered by the blastoderm, and the external YSL (eYSL), which protrudes beyond the blastoderm margin. Only the nuclei of the eYSL are transcriptionally active, being the source of the Nodal signal that diffuses through a small area of the blastoderm at the region of the embryonic shield. All germ layers express similar levels of E-cadherin, but Nodal induces the upregulation in expression of N-cadherin (42). These Nodal-induced cells with higher expression of N-cadherin have higher cell adhesion strengths compared to ectoderm cells (18), and they differentiate into mesendoderm. Those not exposed to the Nodal gradient become ectoderm (43). Furthermore, the Nodal-induced cells with higher N-cadherin levels that differentiate into mesendoderm involute over the blastoderm margin toward the yolk (41,44). However, the mechanism driving this involution and migration due to the regulation of adhesion molecules by Nodal is not completely understood. A cellular Potts model based on biophysical forces could demonstrate zebrafish germ layer involution (18) but without considering the role of the Nodal gradient—new mesendoderm cells with different biophysical properties were created spontaneously at a point in space. Models have been proposed to describe the diffusion of the Nodal gradient (45) but omitting its role in cellular involution. Indeed, the lack of models that can incorporate both biophysical forces such as adhesion and its regulation by morphogen signals prevents us from understanding the interplay between Nodal gradient formation, N-cadherin regulation, and cellular involution during zebrafish gastrulation.

We extend the nondimensional model (Eq. 11) to explain the induction of mesendoderm differentiation, involution, and migration by the diffusion of Nodal and its regulation of N-cadherin (Fig. 4). The 2D model contains a slice of the whole embryo during gastrulation at the germ ring stage, including the yolk, iYSL, eYSL, blastoderm, and enveloping layer (EVL), together with four CAM types: E-cadherin, N-cadherin, and those present in the EVL and yolk (labeled EVL and Yolk in Fig. 4, for simplicity). The equations for CAMs are extended with a regulatory term such that

$$\boldsymbol{c} = (c_1, \ldots, c_n),$$

$$\frac{\partial c_i(\boldsymbol{x}, t)}{\partial t} = -\nabla \cdot (c_i \boldsymbol{V}) + R_{c_i}(\boldsymbol{c}, \boldsymbol{m}), \tag{14}$$

where $\boldsymbol{c}$ is the vector of n CAM type concentrations c_i and $R_{c_i}(\boldsymbol{c}, \boldsymbol{m})$ is the regulation of the CAM type c_i. In addition, the equations for the Nodal morphogen and other regulatory factors are included in a vector $\boldsymbol{m}$ of concentrations of k morphogens and other factors such that

$$\boldsymbol{m} = (m_1, \ldots, m_k),$$

$$\frac{\partial m_i(\boldsymbol{x}, t)}{\partial t} = -\nabla \cdot (m_i \boldsymbol{V}) + \nabla \cdot (D_{m_i} u \nabla m_i) + R_{m_i}(\boldsymbol{c}, \boldsymbol{m}), \tag{15}$$

where D_{m_i} is the diffusion constant per unit of cell density of the morphogen m_i and $R_{m_i}(\boldsymbol{c}, \boldsymbol{m})$ is the regulation of the morphogen m_i expression. Morphogen diffusion depends on cell density because experimental evidence demonstrates that Nodal diffuses through the extracellular space between cells in a tissue (46).

The CAM regulatory terms in $R_{c_i}(\boldsymbol{c}, \boldsymbol{m})$ are all zero for all CAM types c_i, except for N-cadherin, which is regulated by the morphogen Nodal. The expression of N-cadherin in the blastoderm depends on the levels of the morphogen Nodal with a Hill type function such that

$$R_{Ncad}(\boldsymbol{c}, \boldsymbol{m}) = m_{blast} \frac{k_{max}\, m_{nod}^h}{k_{half}^h + m_{nod}^h}, \tag{16}$$

where m_{nod} is the concentration of Nodal, m_{blast} is a molecular marker only present in the blastoderm (as a constant 1), k_{max} is the maximal rate of N-cadherin expression, k_{half} is the concentration of Nodal that yields half the maximal rate, and h is the Hill coefficient.

The model includes the regulatory factors expressed in the iYSL and eYSL regions of the yolk as two lumped variables in $\boldsymbol{m}$ with zero diffusion constant and regulation. Nodal diffuses and is expressed in the eYSL; hence, its diffusion constant is not zero, and its reaction term depends on the eYSL factors in addition to natural degradation, such that

$$R_{nod}(\boldsymbol{c}, \boldsymbol{m}) = k_e m_{eYSL} - \lambda m_{nod}, \tag{17}$$

where k_e is an expression constant, m_{eYSL} is the concentration of eYSL factors, and λ is the decay constant for Nodal.

Substituting Eqs. 16 and 17 in Eqs. 14 and 15, the zebrafish gastrulation model is defined with

$$\frac{\partial u}{\partial t} = -\nabla \cdot (u \boldsymbol{V}),$$

$$\boldsymbol{c} = \left(c_{yolk}, c_{evl}, c_{Ecad}, c_{Ncad}\right),$$

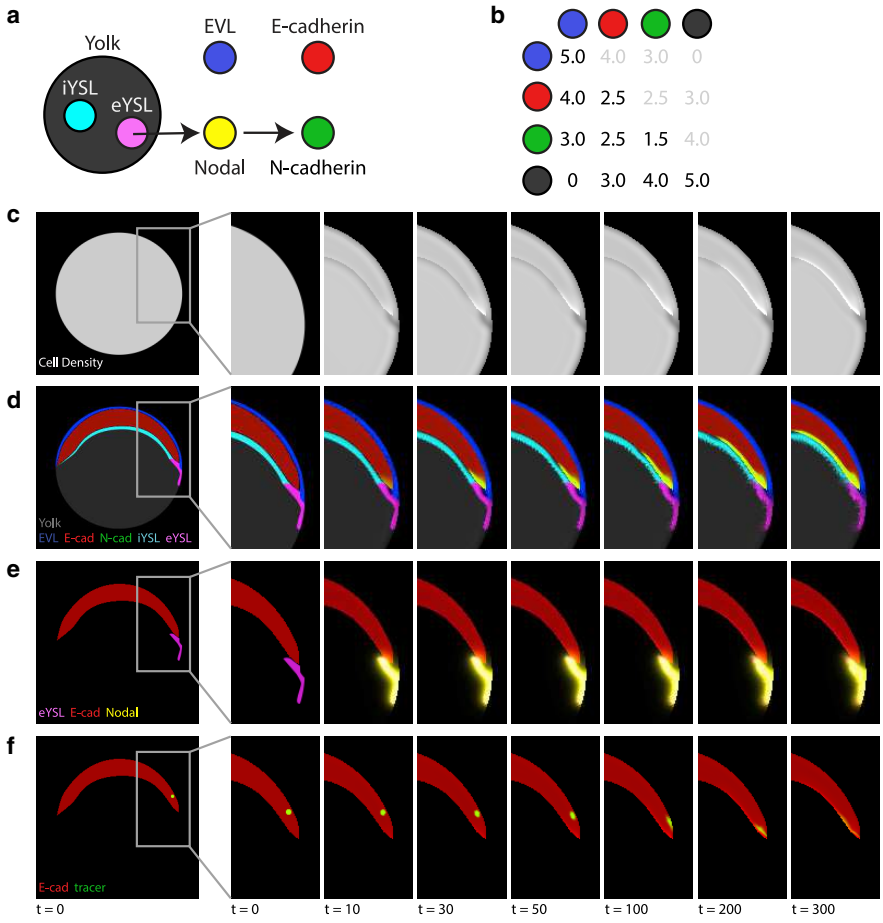

FIGURE 4 Simulation of involution and migration dynamics during zebrafish gastrulation due to the dynamic regulation of CAM expression. (*a*) The regulatory network in the system. iYSL and eYSL regions located in the YSL express nondiffusible factors labeled with the same name (*cyan* and *magenta*, respectively). eYSL factors induce the expression of the diffusible protein Nodal (*yellow*), which induces a higher expression of adhesion protein N-cadherin (*green*). The cells in the EVL produce a specific CAM type (*blue*). All germ layers express the same level of E-cadherin adhesion protein (*red*). (*b*) Adhesion strengths between CAM types. (*c*) The cell density in the embryo is initialized homogenously but dynamically changes because of differences in cell adhesion. (*d*) Mesendodermal progenitors involute from the germ ring toward the animal pole over the margin of the yolk because of the dynamic upregulation of N-cadherin expression. (*e*) Nodal expressed because of eYSL factors in the yolk diffuses to the blastoderm, inducing higher levels of N-cadherin expression in this area, which results in the cells moving toward the animal pole beyond the area of Nodal diffusion. (*f*) A nondiffusible tracer (*green*) is advected by the mesendodermal progenitor cells, showing their involution. The initial state values are zero except at the locations shown (*c–f*, $t = 0$), which are homogeneous with $u_0 = 0.8$, $c_{yolk,0} = 0.8$, $c_{evl,0} = 0.8$, $c_{Ecad,0} = 0.64$, $c_{Ncad,0} = 0.16$, and $m_{iYSL,0} = 0.8$ and $m_{eYSL,0} = 0.8$, $m_{nodal,0} = 0$, and $m_{tracer,0} = 1$. Nondimensional parameter values were $k_{max} = 0.1$, $k_{half} = 0.1$, $h = 2$, $D_{nod} = 1$, $k_e = 10$, and $\lambda = 5$. Domain is of size 25×25 units, discretized into a 250×250 grid; arbitrary units. To see this figure in color, go online.

$$\begin{cases} \dfrac{\partial c_{yolk}}{\partial t} = -\nabla\cdot\left(c_{yolk}\boldsymbol{V}\right), \\ \dfrac{\partial c_{evl}}{\partial t} = -\nabla\cdot\left(c_{evl}\boldsymbol{V}\right), \\ \dfrac{\partial c_{Ecad}}{\partial t} = -\nabla\cdot\left(c_{Ecad}\boldsymbol{V}\right), \\ \dfrac{\partial c_{Ncad}}{\partial t} = -\nabla\cdot\left(c_{Ncad}\boldsymbol{V}\right) + m_{blast}\,\dfrac{k_{max}\,m_{nod}^{h}}{k_{half}^{h} + m_{nod}^{h}}, \end{cases}$$

$$\boldsymbol{m} = \left(m_{iYSL}, m_{eYSL}, m_{nod}\right),$$

The parameters of the model were estimated based on experimental data and physical constraints. The adhesion parameters between N-cadherin and E-cadherin were derived from atomic force microscopy data from zebrafish ectoderm, mesoderm, and endoderm cells (18). We assumed that mesendoderm cells express both N-cadherin and E-cadherin, whereas ectoderm cells express only E-cadherin (18,42). Homotypic adhesions for cells in the EVL were set to an arbitrary high value because this region is expected to remain clustered together. Similarly, the homotypic adhesion of the yolk was set to the same high value to simulate a single cohesive yolk cell. Heterotypic adhesion between yolk and EVL was set to zero for simplicity. Following

$$\begin{cases} \dfrac{\partial m_{iYSL}}{\partial t} = -\nabla\cdot\left(m_{iYSL}\boldsymbol{V}\right), \\ \dfrac{\partial m_{eYSL}}{\partial t} = -\nabla\cdot\left(m_{eYSL}\boldsymbol{V}\right), \\ \dfrac{\partial m_{nod}}{\partial t} = -\nabla\cdot\left(m_{nod}\boldsymbol{V}\right) + \nabla\cdot\left(D_{nod}u\nabla m_{nod}\right) + k_e m_{eYSL} - \lambda m_{nod}. \end{cases} \tag{18}$$

the same assumptions as (18), heterotypic adhesions between N-cadherin and E-cadherin and the inner yolk and outer EVL were set such that N-cadherin preferentially adhered to the yolk over the EVL, whereas E-cadherin preferentially adhered to the EVL over the yolk. The specific adhesion constants used between all CAM types are shown in Fig. 4 *b*. Constants D_{nod}, k_e, and λ govern the Nodal gradient and were estimated for the resulting Nodal gradient to span between the eYSL and the EVL. The Hill coefficient h was set to 2 for simplicity; k_{max} and k_{half} were estimated to result in moderate N-cadherin expression levels.

The simulation initial state is based on experimental images of zebrafish gastrulation (44,47). The embryo is defined with a homogeneous cell density circle (Fig. 4 *c*, $t = 0$). Within the embryo, the initial EVL and Yolk CAM densities are set at the locations of the EVL and yolk, respectively, while the E-cadherin and N-cadherin are set in the blastoderm area, with E-cadherin being higher than N-cadherin (Fig. 4 *d*, $t = 0$), as it has been shown experimentally (18,42). The factors iYSL and eYSL are initialized homogeneously in their respective regions (Fig. 4 *d*, $t = 0$) while Nodal is initially zero along all the domain (Fig. 4 *e*, $t = 0$). A zero-flux boundary was imposed at the interface between the blastoderm with the EVL and yolk regions to simulate the sealing between EVL cells via apical junctional complexes (48) and the dense cortical yolk cell cytoskeleton (49), respectively. For simplicity, the simulation does not include the EVL cell migration over the yolk.

Fig. 4, *c–f* show the simulation of zebrafish gastrulation, during which the mesendoderm progenitors involute and migrate over the margin of the yolk because of the dynamic regulation of CAM expression by the diffusing morphogen Nodal. The eYSL factors activate the expression of Nodal in the eYSL region of the yolk, which then diffuses through the germ ring region of the blastoderm, causing the upregulation of N-cadherin in the cells at this location (Fig. 4 *e*). The increased concentration of N-cadherin causes an increase of adhesive forces, which results in the involution and migration of these cells toward the animal pole. Crucially, even after the cells leave the region where Nodal diffuses and stop expressing additional N-cadherin, they continue migrating toward the animal pole because the movement is driven by the acquired higher adhesion strength (as a simplification, the model omits further regulation and degradation of N-cadherin). As these cells migrate, additional cells closer to the EVL fill the vacated space and are hence exposed to Nodal signals, resulting in further involution dynamics. A nondiffusible tracer in the simulation (Fig. 4 *f*) shows the involution movement of the cells and their movement along the margin of the yolk. In this way, the model shows how the dynamic regulation of CAM expression can cause specific patterns and cellular behaviors during gastrulation that are essential for the correct development of the embryo.

To determine the sensitivity of the model parameters, we performed a parameter scan over the five parameters governing Nodal expression and its downstream response. Fig. 5 shows the resulting spatial concentration levels of N-cadherin and Nodal when increasing or decreasing each parameter individually. Inhibition of Nodal signaling

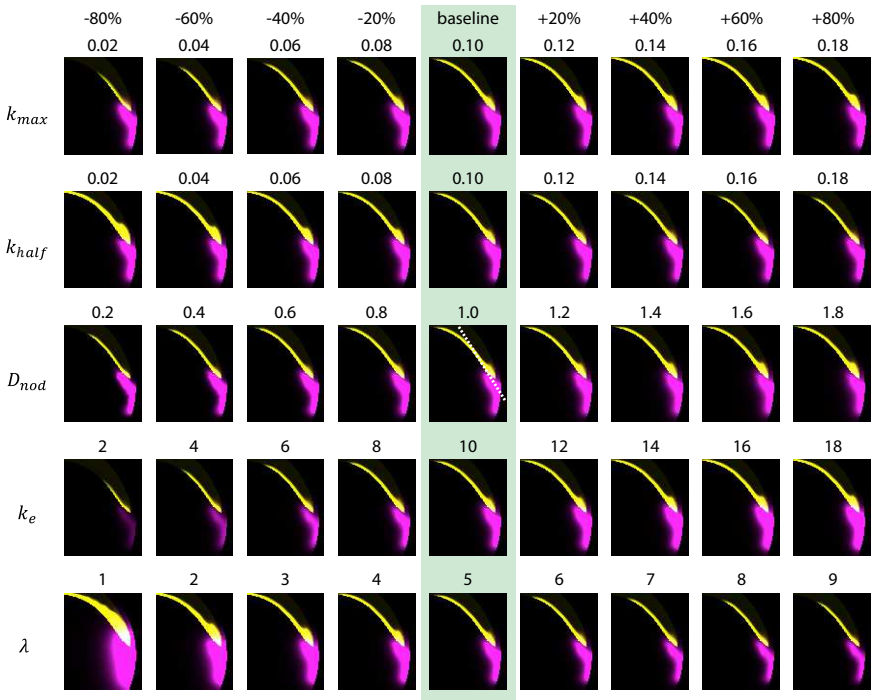

FIGURE 5 Resulting expression patterns of N-cadherin as modulated by the parameters controlling Nodal expression and its regulatory effects on N-cadherin. Each simulation corresponds to the percentage perturbation indicated in the column to the parameter in the row and resulting in the value above each plot. First two rows vary the regulatory effect of Nodal (*magenta*) in the expression of N-cadherin (*yellow*). Last three rows vary the concentration gradient formed by Nodal. All simulations are shown at $t = 300$, arbitrary units. White dotted line in center simulation shows the location of the profile plots in Fig. 6. To see this figure in color, go online.

reduces N-cadherin expression along both the emerging anterior-posterior (AP) and dorso-ventral (DV) axes. Slight reductions in the extent of the Nodal gradient cause reduction of N-cadherin expression along the DV axis, and larger reductions in Nodal expression cause reduction along the AP axis, preventing the region of high N-cadherin concentration from reaching the animal pole. These behaviors are consistent with changes in expression of zebrafish mesendoderm markers due to experimental inhibition of Nodal signaling in vivo (50). In addition, removing Nodal signaling and instead including a cell population with high N-cadherin levels results in a thin layer near the region of the yolk and no involution behavior (Fig. S4).

The model shows how Nodal can upregulate N-cadherin to cause these cells to migrate to the animal pole, resulting in cells with high N-cadherin expression levels even beyond the expression gradient of Nodal. The extent of this behavior is modulated by both the parameters controlling the strength of Nodal upregulating N-cadherin and those controlling the expression gradient of Nodal, as shown in the spatial phenotypes as profile plots in Fig. 6. The concentration levels of Nodal and N-cadherin can increase or decrease by varying the different parameters, yet all simulations show how the expression pattern of N-cadherin goes beyond that of Nodal because of the migration of the cells to the animal pole after acquiring higher adhesion strengths to the yolk, demonstrating the robustness of the system along large parameter ranges. In addition, N-cadherin needs to have a higher adhesion strength to the yolk than E-cadherin because simulations with equal adhesion strengths between all CAMs (Fig. S5) results in no involution, a behavior that can be rescued by just increasing the adhesion strength between N-cadherin and the yolk (Fig. S6) but not by increasing the adhesion strength between E-cadherin and the yolk (Fig. S7).

We tested whether the dynamic regulation of N-cadherin by Nodal was necessary for the zebrafish involution behavior with simulations adapting a continuous modeling approach using discrete cell types with different adhesion strengths (26,27). We implemented an equivalent 2D zebrafish model based on different cell types with inherent adhesion strengths between them (see Supporting Materials and Methods). The diffusive gradient of Nodal now directly induces the differentiation of ectoderm cells into mesendoderm cells, which have a higher adhesion strength to the yolk. The results show that with the experimental adhesion strengths the differentiated mesendoderm cells did not adhere to the yolk but diffused through the blastoderm (Fig. S8), whereas the tracer migrated upwards toward the animal pole rather than involuting as expected (Fig. S9), even with the correct patterns of Nodal gradient (Fig. S10). Increasing the adhesion strength between the

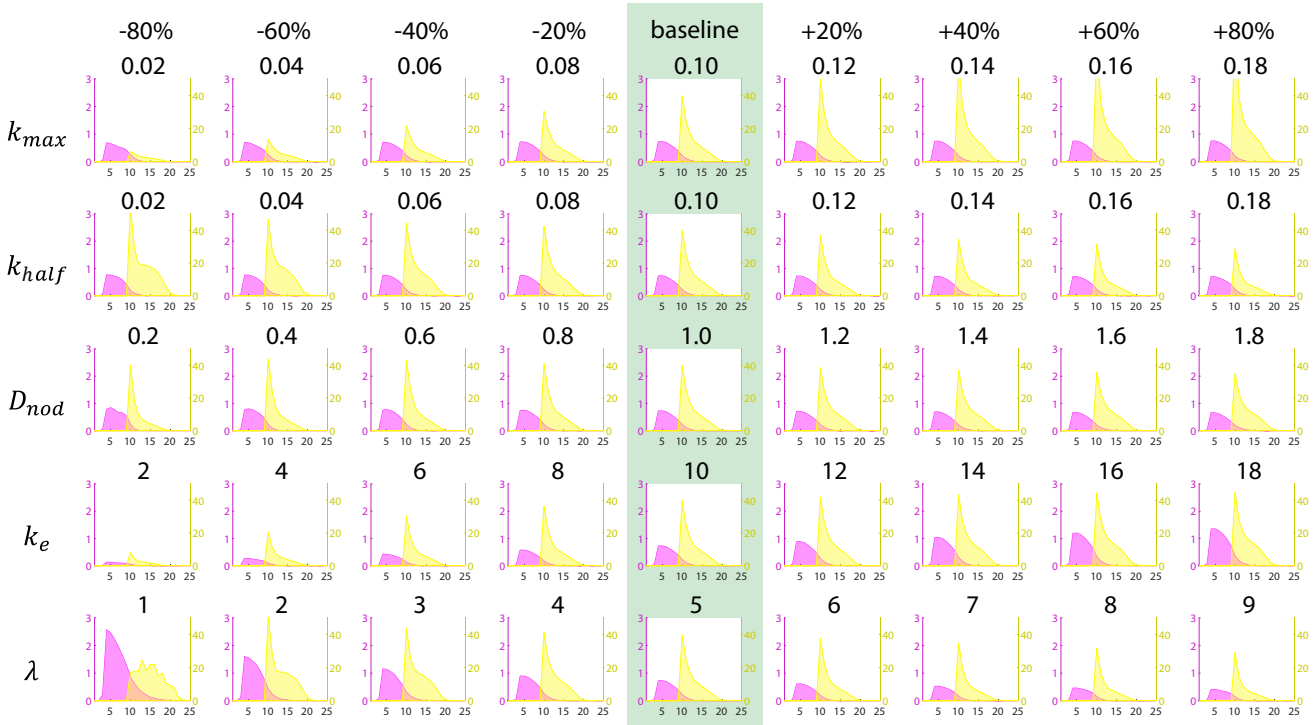

FIGURE 6 Profile plots of the concentration levels of Nodal and N-cadherin resulting from different parameters. N-cadherin (*yellow*) expression pattern extends beyond the Nodal (*magenta*) concentration gradient due to the cell movements toward the animal pole caused by differential adhesion strengths. Each profile plot corresponds to the concentration level of Nodal and N-cadherin along a line through the eYSL and blastoderm (animal pole to the *right*) as shown in Fig. 5 center plot and with the parameter indicated in the row perturbed by the percentage indicated in the column resulting in the value above each plot. All simulations are shown at $t = 300$, arbitrary units. To see this figure in color, go online.

yolk and the differentiated mesendoderm cells resulted in a very thin layer of mesendoderm cells over the margin of the yolk because of the instantaneous change in adhesion strength in these cells that translates into an instantaneous very strong adhesion force toward the yolk, as highlighted by the radial movements of the tracer directly toward the yolk without involuting near the eYSL (Fig. S9). This is in contrast to the proposed model of dynamic adhesion regulation, in which the gradual change in cell adhesion strengths results in the expected band of involuted cells and involution dynamics of the tracer (Fig. 4).

DISCUSSION

Here, we presented a novel, to our knowledge, continuous mathematical model of cell-cell adhesion due to the explicit expression and regulation of cell adhesion proteins (CAMs) for the explanation of sorting, intercalation, and convolution cellular behaviors. Cells express different CAM types, which have specific adhesive properties when binding to CAMs of the same or different type. The adhesive forces between CAMs produce cell movements dependent on the cell density and CAM concentration in neighbor cells within a sensing radius. Moving cells carry their expressed CAMs and possibly other factors with them. CAM expression can be regulated by intra- and extracellular factors, including diffusible morphogens such as Nodal. Because regulation alters the expression level of specific CAM types, the adhesive properties of cells are defined dynamically. In this way, the regulatory dynamics of CAM expression can dictate the resulting tissue patterns and shapes.

The capacity of the model to explain cellular in vitro and in vivo behaviors were demonstrated with three sets of numerical experiments showing sorting, intercalation, and convolution spatial dynamics. First, we showed how this approach could recapitulate the classical sorting behaviors in a model of spatially randomized cells expressing one of two different CAM types. The simulations showed how the emergent sorting dynamics displayed by the cell populations—engulfment, partial engulfment, mixing, or complete sorting—depended on the homotypic and heterotypic adhesion strengths between the CAM types. Next, we showed how intercalation dynamics in a growing cell population depended on the type of CAMs expressed and their adhesion strengths. When the two proliferating populations expressed the same CAM type, they formed a completely separated boundary between them. However, when the two proliferating populations expressed different CAM types, they intercalated at the boundary. The intercalation interface shows a characteristic amplitude and wavelength, which the model predicts depending on specific physical cellular parameters. These predictions could be tested in vitro by recording the amplitude and wavelength of the intercalation interface formed between different cell types with known physical properties. Most notably, the cell-sensing radius is predicted to correlate with the intercalation wavelength, whereas the cell growth rate is predicted to inversely correlate with the intercalation amplitude.

Importantly, the dynamic regulation of CAMs can be explicitly included in the proposed model, as it is essential in many in vivo behaviors. We demonstrated this capacity in the last experiment, which showed cellular involution behaviors controlled by a diffusible morphogen during zebrafish gastrulation, a behavior that could not be recapitulated with a model based on discrete cell types. The model included the expression and diffusion of the morphogen Nodal, which formed a concentration gradient extending toward the blastoderm. Nodal induced the upregulation of N-cadherin, implicitly changing the adhesive properties of these cells. These new adhesive properties resulted in cellular involution and migration over the margin of the yolk, a movement that continued beyond the Nodal gradient because of the properties of the new CAM expression levels, which need to have differential adhesion strengths. The precise concentration profiles formed by Nodal and N-cadherin because of their dynamic regulation modulating adhesion forces were investigated by varying the parameters of the pathway through large ranges. Crucially, the system showed that the dynamic regulation by Nodal was necessary to induce the involution behavior and how the expression pattern of N-cadherin robustly extended beyond the gradient of Nodal over these parameter ranges, a prediction by the model to be tested in vivo. A reporter system has been developed to visualize Nodal gradients in zebrafish by inserting a GFP tag into the zebrafish Nodal ligands (51) and used to measure the diffusion of ectopic Nodal (45). Future work could test the model predictions and fit the key parameters by visualizing the endogenous Nodal gradient together with N-cadherin expression during zebrafish gastrulation to provide deeper insights into the mechanisms controlling zebrafish embryogenesis.

Previous continuous modeling approaches have replicated cellular behaviors due to cell-cell adhesion by modeling cell types with specific adhesion properties. Continuous models of cell-cell adhesion have demonstrated cell sorting (26) and intercalation (27) dynamics by explicitly modeling two distinct cellular populations with different cell-cell adhesion constants. Similarly, proposed continuous models of tumor dynamics include static adhesion coefficients defined between cancer cells and the extracellular matrix (29). Other continuous approaches have modeled separated cellular populations representing different cell types, in which one cell population could transition to another one as when acquiring a mutation (32), but the adhesive properties between each population are still predefined and static. Although these models are excellent approaches for simulating large cellular populations with static adhesive properties, they are limited in their capacity to model dynamic adhesive behaviors. In contrast, the continuous model presented here can explain the behaviors

of both cell populations with static adhesive properties (simulations 1 and 2) and those with dynamically regulated adhesive properties (simulation 3) by directly including the expression and concentrations of CAMs. The dynamic regulation of CAMs is a key element in many biological processes, as we demonstrated here, and, to our knowledge, has previously only been captured with hybrid models (25). However, numerically solving hybrid models are computationally infeasible for large cell numbers, and their mathematical analysis is limited because of their discrete nature. Computing a cell-sorting simulation takes 4 h using one core with the presented continuous framework but 24 h using 16 cores with a discrete cellular Potts model implementation (24,52).

The presented model only accounts for cell motilities due to dispersion and directed adhesion forces, but it could be extended to incorporate other active motility mechanisms. Extended Viscek models taking into account intrinsic cell motilities and alignment interactions have been shown to be sufficient to exhibit cell-sorting behaviors (53). This phenomenon could be incorporated into the model with an additional nonlocal term depending on the velocity of neighboring cells. In addition, other intrinsic cell motility forces could be incorporated into the velocity term of the cell density, such as chemotactic behaviors, which are easily incorporated in continuous models (54).

The proposed approach uses adhesion forces that arise dynamically from CAM expression instead of from explicit cell types. Single-cell force spectroscopy can directly measure the adhesion forces between cells expressing different levels of CAMs (55), which can be used to experimentally set the parameters of the model. For simplicity, the model assume that the binding forces are proportional to the product of the relative concentration of CAMs; however, more complex formulations of adhesion ligands and receptors are also possible (56). The extracellular matrix is an additional important element in cell-cell adhesion dynamics, and it could be incorporated into the continuous model of adhesion (29). Together with adhesion forces, cell cortex elasticity and tension also can play a role in certain behaviors and be essential during tissue shape dynamics (18,57). Future work will extend the presented model to incorporate the role of these components in cellular behaviors.

The regulation of CAM expression and how these molecules affect large-scale cellular behaviors is extraordinarily important in both healthy and diseased states (58–60). The proposed model integrates genetic regulation of CAMs, the biophysical forces of adhesion that drive cell motion, and the subsequent cellular dynamics. This integrated view of dynamic adhesion will be essential for understanding tissue behaviors in developmental and cancer biology as well as in bioengineering (61–63). The proposed continuum approach allows for the simulation of large cell populations (up to the whole-organism scale), as well as the continuous phenomena involved in genetic regulation (e.g., morphogen gradients and CAM expression). Crucially, machine learning approaches for the reverse-engineering of the regulation of patterning (64–66) and cancer formation (67,68) directly from formalized experimental data (69–72) can be integrated with the proposed model, with the goal to discover the specific regulatory mechanisms of CAMs that give rise to key spatial phenotypes. In summary, the presented continuous modeling approach will pave the way for the understanding of the regulatory dynamics of cell adhesion essential in developmental, regenerative, and cancer biology.

SUPPORTING MATERIAL

Supporting Material can be found online at https://doi.org/10.1016/j.bpj.2019.10.032.

APPENDIX: NUMERICAL METHODS

Numerical simulations were performed in a 2D domain using the explicit upwind finite volume method with flux limiting in a uniform square lattice and a zero-flux boundary condition. The fluxes between control volumes due to the adhesion velocity (Eq. 6) are computed at four points A–D, one at each face midpoint (Fig. 1 *b*). At each of these midpoints and for each pair of CAMs, the nonlocal integral term for adhesion (Eq. 7) is computed within a circle with radius R and centered at the face point (Fig. 1 *c*). The integral circle is discretized with parameters N_r, $N_\theta \in \mathbb{N}$, defining a set of points uniformly distributed along N_r radial values and $4(i_r N_\theta / 4N_r) + 2$ angular values for each radial value $i_r \in \mathbb{N}$, $1 \leq i_r \leq N_r$, as in (27). Because the cell density and CAM concentrations are numerically defined at the control volume centers, bilinear interpolation is used from the four surrounding control volume centers to calculate their values at the regular integral points in the circle (*red points* and *color lines* in Fig. 1 *c*) and the average from the two surrounding control volume centers to calculate their values at the face point (*black point* in Fig. 1 *c*). The bilinear interpolations of the integral circle are precomputed in a weight matrix representing a kernel, which then are used to efficiently calculate the adhesion velocities in each face midpoint with a kernel convolution operation (because of symmetry, the kernel for points C and D is the transpose of the kernel for points A and B). Cell densities and CAM concentrations outside of the domain are considered zero in the kernel convolution operation, as is consistent with the zero-flux boundary condition (73). The system was numerically solved with a generalized Runge-Kutta fourth-order solver using ROWMAP (33). Simulation computations used MATLAB R2017b (The MathWorks).

AUTHOR CONTRIBUTIONS

J.M.K. and D.L. designed the study, developed the models, analyzed the data, and wrote the manuscript. J.M.K. performed the simulations. D.L. secured funding.

ACKNOWLEDGMENTS

We thank Bradford Peercy for critical comments on the article and the members of the Lobo Lab for helpful discussions.

This work was supported by the National Science Foundation under grant IIS-1566077. Computations used the University of Maryland, Baltimore

County (UMBC) High Performance Computing Facility, supported by the National Science Foundation grants OAC-1726023, CNS-0821258, CNS-1228778, and DMS-0821311, and UMBC.

REFERENCES

1. Foty, R. A., and M. S. Steinberg. 2013. Differential adhesion in model systems. *Wiley Interdiscip. Rev. Dev. Biol.* 2:631–645.
2. Townes, P. L., and J. Holtfreter. 1955. Directed movements and selective adhesion of embryonic amphibian cells. *J. Exp. Zool.* 128:53–120.
3. Steinberg, M. S. 1958. On the chemical bonds between animal cells. A mechanism for type-specific association. *Am. Nat.* 92:65–81.
4. Maître, J. L., and C. P. Heisenberg. 2013. Three functions of cadherins in cell adhesion. *Curr. Biol.* 23:R626–R633.
5. Samanta, D., and S. C. Almo. 2015. Nectin family of cell-adhesion molecules: structural and molecular aspects of function and specificity. *Cell. Mol. Life Sci.* 72:645–658.
6. Togashi, H., K. Kominami, …, Y. Takai. 2011. Nectins establish a checkerboard-like cellular pattern in the auditory epithelium. *Science.* 333:1144–1147.
7. Bruner, H. C., and P. W. B. Derksen. 2018. Loss of E-cadherin-dependent cell-cell adhesion and the development and progression of cancer. *Cold Spring Harb. Perspect. Biol.* 10:a029330.
8. Fuhrmann, A., A. Banisadr, …, A. J. Engler. 2017. Metastatic state of cancer cells may be indicated by adhesion strength. *Biophys. J.* 112:736–745.
9. Thiery, J. P., H. Acloque, …, M. A. Nieto. 2009. Epithelial-mesenchymal transitions in development and disease. *Cell.* 139:871–890.
10. Xing, J., and X. J. Tian. 2019. Investigating epithelial-to-mesenchymal transition with integrated computational and experimental approaches. *Phys. Biol.* 16:031001.
11. Wada, N. 2011. Spatiotemporal changes in cell adhesiveness during vertebrate limb morphogenesis. *Dev. Dyn.* 240:969–978.
12. Ahrens, M. J., Y. Li, …, A. T. Dudley. 2009. Convergent extension movements in growth plate chondrocytes require gpi-anchored cell surface proteins. *Development.* 136:3463–3474.
13. Seguin, L., J. S. Desgrosellier, …, D. A. Cheresh. 2015. Integrins and cancer: regulators of cancer stemness, metastasis, and drug resistance. *Trends Cell Biol.* 25:234–240.
14. Hiratsuka, S., S. Goel, …, R. K. Jain. 2011. Endothelial focal adhesion kinase mediates cancer cell homing to discrete regions of the lungs via E-selectin up-regulation. *Proc. Natl. Acad. Sci. USA.* 108:3725–3730.
15. Tai, Y. L., L. C. Chen, and T. L. Shen. 2015. Emerging roles of focal adhesion kinase in cancer. *BioMed Res. Int.* 2015:690690.
16. Graner, F., and J. A. Glazier. 1992. Simulation of biological cell sorting using a two-dimensional extended Potts model. *Phys. Rev. Lett.* 69:2013–2016.
17. Glazier, J. A., and F. Graner. 1993. Simulation of the differential adhesion driven rearrangement of biological cells. *Phys. Rev. E Stat. Phys. Plasmas Fluids Relat. Interdiscip. Topics.* 47:2128–2154.
18. Krieg, M., Y. Arboleda-Estudillo, …, C. P. Heisenberg. 2008. Tensile forces govern germ-layer organization in zebrafish. *Nat. Cell Biol.* 10:429–436.
19. Zajac, M., G. L. Jones, and J. A. Glazier. 2003. Simulating convergent extension by way of anisotropic differential adhesion. *J. Theor. Biol.* 222:247–259.
20. Gerisch, A., and K. J. Painter. 2010. Mathematical modeling of cell adhesion and its applications to developmental biology and cancer invasion. *In* Cell Mechanics: From Single Scale-Based Models to Multiscale Modelling. A. Chauvière, L. Preziosi, and C. Verdier, eds. CRC Press, pp. 319–350.
21. Glazier, J. A., Y. Zhang, …, S. Schnell. 2008. Coordinated action of N-CAM, N-cadherin, EphA4, and ephrinB2 translates genetic prepatterns into structure during somitogenesis in chick. *Curr. Top. Dev. Biol.* 81:205–247.
22. Turner, S., and J. A. Sherratt. 2002. Intercellular adhesion and cancer invasion: a discrete simulation using the extended Potts model. *J. Theor. Biol.* 216:85–100.
23. Anderson, A. R. 2005. A hybrid mathematical model of solid tumour invasion: the importance of cell adhesion. *Math. Med. Biol.* 22:163–186.
24. Zhang, Y., G. L. Thomas, …, J. A. Glazier. 2011. Computer simulations of cell sorting due to differential adhesion. *PLoS One.* 6:e24999.
25. Ramis-Conde, I., D. Drasdo, …, M. A. Chaplain. 2008. Modeling the influence of the E-cadherin-beta-catenin pathway in cancer cell invasion: a multiscale approach. *Biophys. J.* 95:155–165.
26. Armstrong, N. J., K. J. Painter, and J. A. Sherratt. 2006. A continuum approach to modelling cell-cell adhesion. *J. Theor. Biol.* 243:98–113.
27. Murakawa, H., and H. Togashi. 2015. Continuous models for cell-cell adhesion. *J. Theor. Biol.* 374:1–12.
28. Armstrong, N. J., K. J. Painter, and J. A. Sherratt. 2009. Adding adhesion to a chemical signaling model for somite formation. *Bull. Math. Biol.* 71:1–24.
29. Gerisch, A., and M. A. Chaplain. 2008. Mathematical modelling of cancer cell invasion of tissue: local and non-local models and the effect of adhesion. *J. Theor. Biol.* 250:684–704.
30. Kim, Y., S. Lawler, …, A. Friedman. 2009. A mathematical model for pattern formation of glioma cells outside the tumor spheroid core. *J. Theor. Biol.* 260:359–371.
31. Painter, K. J., N. J. Armstrong, and J. A. Sherratt. 2010. The impact of adhesion on cellular invasion processes in cancer and development. *J. Theor. Biol.* 264:1057–1067.
32. Domschke, P., D. Trucu, …, M. A J Chaplain. 2014. Mathematical modelling of cancer invasion: implications of cell adhesion variability for tumour infiltrative growth patterns. *J. Theor. Biol.* 361:41–60.
33. Weiner, R., B. A. Schmitt, and H. Podhaisky. 1997. ROWMAP–a ROW-code with Krylov techniques for large stiff ODEs. *Appl. Numer. Math.* 25:303–319.
34. Steinberg, M. S. 1963. Reconstruction of tissues by dissociated cells. Some morphogenetic tissue movements and the sorting out of embryonic cells may have a common explanation. *Science.* 141:401–408.
35. Armstrong, P. B. 1971. Light and electron microscope studies of cell sorting in combinations of chick embryo neural retina and retinal pigment epithelium. *Wilhelm Roux Arch. Entwickl. Mech. Org.* 168:125–141.
36. Cochet-Escartin, O., T. T. Locke, …, E. S. Collins. 2017. Physical mechanisms driving cell sorting in hydra. *Biophys. J.* 113:2827–2841.
37. Katsamba, P., K. Carroll, …, B. H. Honig. 2009. Linking molecular affinity and cellular specificity in cadherin-mediated adhesion. *Proc. Natl. Acad. Sci. USA.* 106:11594–11599.
38. Alber, M. S., M. A. Kiskowski, …, Y. I. Jiang. 2003. On cellular automaton approaches to modeling biological cells. *In* Mathematical Systems Theory in Biology, Communications, Computation, and Finance. J. Rosenthal and D. S. Gilliam, eds. Springer-Verlag, pp. 1–39.
39. Harrison, O. J., J. Vendome, …, L. Shapiro. 2012. Nectin ectodomain structures reveal a canonical adhesive interface. *Nat. Struct. Mol. Biol.* 19:906–915.
40. Schier, A. F. 2009. Nodal morphogens. *Cold Spring Harb. Perspect. Biol.* 1:a003459.
41. Carvalho, L., and C. P. Heisenberg. 2010. The yolk syncytial layer in early zebrafish development. *Trends Cell Biol.* 20:586–592.
42. Giger, F. A., and N. B. David. 2017. Endodermal germ-layer formation through active actin-driven migration triggered by N-cadherin. *Proc. Natl. Acad. Sci. USA.* 114:10143–10148.
43. Rodaway, A., H. Takeda, …, N. Holder. 1999. Induction of the mesendoderm in the zebrafish germ ring by yolk cell-derived TGF-beta family signals and discrimination of mesoderm and endoderm by FGF. *Development.* 126:3067–3078.

44. Montero, J. A., L. Carvalho, …, C. P. Heisenberg. 2005. Shield formation at the onset of zebrafish gastrulation. *Development.* 132:1187–1198.

45. Wang, Y., X. Wang, …, K. Sampath. 2016. Extracellular interactions and ligand degradation shape the nodal morphogen gradient. *eLife.* 5:1–19.

46. Williams, P. H., A. Hagemann, …, J. C. Smith. 2004. Visualizing long-range movement of the morphogen Xnr2 in the Xenopus embryo. *Curr. Biol.* 14:1916–1923.

47. Lachnit, M., E. Kur, and W. Driever. 2008. Alterations of the cytoskeleton in all three embryonic lineages contribute to the epiboly defect of Pou5f1/Oct4 deficient MZspg zebrafish embryos. *Dev. Biol.* 315:1–17.

48. Slanchev, K., T. J. Carney, …, M. Hammerschmidt. 2009. The epithelial cell adhesion molecule EpCAM is required for epithelial morphogenesis and integrity during zebrafish epiboly and skin development. *PLoS Genet.* 5:e1000563.

49. Bruce, A. E. 2016. Zebrafish epiboly: spreading thin over the yolk. *Dev. Dyn.* 245:244–258.

50. Mizoguchi, T., T. Izawa, …, Y. Kikuchi. 2006. Fgf signaling negatively regulates Nodal-dependent endoderm induction in zebrafish. *Dev. Biol.* 300:612–622.

51. Jing, X. H., S. M. Zhou, …, Y. Chen. 2006. Mechanisms underlying long- and short-range nodal signaling in Zebrafish. *Mech. Dev.* 123:388–394.

52. Chen, N., J. A. Glazier, …, M. S. Alber. 2007. A parallel implementation of the Cellular Potts Model for simulation of cell-based morphogenesis. *Comput. Phys. Commun.* 176:670–681.

53. Belmonte, J. M., G. L. Thomas, …, H. Chaté. 2008. Self-propelled particle model for cell-sorting phenomena. *Phys. Rev. Lett.* 100:248702.

54. Hillen, T., and K. J. Painter. 2009. A user's guide to PDE models for chemotaxis. *J. Math. Biol.* 58:183–217.

55. Malek-Zietek, K. E., M. Targosz-Korecka, and M. Szymonski. 2017. The impact of hyperglycemia on adhesion between endothelial and cancer cells revealed by single-cell force spectroscopy. *J. Mol. Recognit.* 30:e2628.

56. Xu, H., and D. E. Shaw. 2016. A simple model of multivalent adhesion and its application to influenza infection. *Biophys. J.* 110:218–233.

57. Manning, M. L., R. A. Foty, …, E. M. Schoetz. 2010. Coaction of intercellular adhesion and cortical tension specifies tissue surface tension. *Proc. Natl. Acad. Sci. USA.* 107:12517–12522.

58. Iwamoto, D. V., and D. A. Calderwood. 2015. Regulation of integrin-mediated adhesions. *Curr. Opin. Cell Biol.* 36:41–47.

59. Teo, W. W., V. F. Merino, …, S. Sukumar. 2016. HOXA5 determines cell fate transition and impedes tumor initiation and progression in breast cancer through regulation of E-cadherin and CD24. *Oncogene.* 35:5539–5551.

60. Ito, K., S. H. Park, …, H. Y. Irie. 2016. PTK6 inhibition suppresses metastases of triple-negative breast cancer via SNAIL-dependent E-cadherin regulation. *Cancer Res.* 76:4406–4417.

61. Glass, D. S., and I. H. Riedel-Kruse. 2018. A synthetic bacterial cell-cell adhesion toolbox for programming multicellular morphologies and patterns. *Cell.* 174:649–658.e16.

62. Toda, S., L. R. Blauch, …, W. A. Lim. 2018. Programming self-organizing multicellular structures with synthetic cell-cell signaling. *Science.* 361:156–162.

63. Herath, S., and D. Lobo. 2019. Cross-inhibition of Turing patterns explains the self-organized regulatory mechanism of planarian fission. *J. Theor. Biol.* 485:110042.

64. Lobo, D., and M. Levin. 2015. Inferring regulatory networks from experimental morphological phenotypes: a computational method reverse-engineers planarian regeneration. *PLoS Comput. Biol.* 11: e1004295.

65. Lobo, D., J. Morokuma, and M. Levin. 2016. Computational discovery and in vivo validation of hnf4 as a regulatory gene in planarian regeneration. *Bioinformatics.* 32:2681–2685.

66. Lobo, D., and M. Levin. 2017. Computing a worm: reverse-engineering planarian regeneration. *In* Advances in Unconventional Computing. Volume 2: Prototypes, Models and Algorithms. A. Adamatzky, ed. Springer International Publishing, pp. 637–654.

67. Lobikin, M., D. Lobo, …, M. Levin. 2015. Serotonergic regulation of melanocyte conversion: a bioelectrically regulated network for stochastic all-or-none hyperpigmentation. *Sci. Signal.* 8:ra99.

68. Lobo, D., M. Lobikin, and M. Levin. 2017. Discovering novel phenotypes with automatically inferred dynamic models: a partial melanocyte conversion in Xenopus. *Sci. Rep.* 7:41339.

69. Lobo, D., E. B. Feldman, …, M. Levin. 2014. A bioinformatics expert system linking functional data to anatomical outcomes in limb regeneration. *Regeneration (Oxf.).* 1:37–56.

70. Lobo, D., T. J. Malone, and M. Levin. 2013. Towards a bioinformatics of patterning: a computational approach to understanding regulative morphogenesis. *Biol. Open.* 2:156–169.

71. Lobo, D., T. J. Malone, and M. Levin. 2013. Planform: an application and database of graph-encoded planarian regenerative experiments. *Bioinformatics.* 29:1098–1100.

72. Lobo, D., E. B. Feldman, …, M. Levin. 2014. Limbform: a functional ontology-based database of limb regeneration experiments. *Bioinformatics.* 30:3598–3600.

73. Gerisch, A. 2010. On the approximation and efficient evaluation of integral terms in PDE models of cell adhesion. *IMA J. Numer. Anal.* 30:173–194.